atmosphere

MDPI

Article

Research on Lidar Network Observation of Aerosol and Pollution in Beijing 2022 Winter Olympics

Tong Lu [1,2], Zhigang Li [1,*], Yubao Chen [2,*], Zhichao Bu [2] and Xiaopeng Wang [2]

[1] College of Physics and Optoelectronic Engineering, Ludong University, Yantai 264025, China
[2] Meteorological Observation Center, China Meteorological Administration, Beijing 100081, China
* Correspondence: lizg_ldu@126.com (Z.L.); yubao_chen@aliyun.com (Y.C.)

Abstract: During the Beijing Winter Olympics, three sets of aerosol lidar in different regions were used to conduct continuous observations to study the optical properties and vertical distribution characteristics of atmospheric aerosol. Based on the lidar data and sun photometer data, the accurate lidar ratio was determined to improve the inversion accuracy of the aerosol backscattering coefficient. The influence of meteorological conditions such as temperature, relative humidity, wind speed, and wind direction on the optical properties of aerosol were analyzed, and the type of aerosol was classified by the depolarization ratio of aerosol particles and CALIPSO data. Furthermore, the backward trajectory analysis, potential source contribution function (PSCF), and concentration weighted trajectories (CWT) were employed to explore the sources and transport mechanisms of pollutants. The analysis found that the extinction coefficient under the atmospheric boundary layer during the Winter Olympics had a spatial distribution pattern of high value in the southeast and low value in the northwest. The occurrence of aerosol pollution events is not only caused by local emissions, but is also related to regional transmission.

Keywords: Winter Olympics; lidar; aerosol; optical properties; vertical distribution

Citation: Lu, T.; Li, Z.; Chen, Y.; Bu, Z.; Wang, X. Research on Lidar Network Observation of Aerosol and Pollution in Beijing 2022 Winter Olympics. *Atmosphere* **2022**, *13*, 1901. https://doi.org/10.3390/atmos13111901

Academic Editor: Pavel Mikuška

Received: 29 September 2022
Accepted: 7 November 2022
Published: 14 November 2022

1. Introduction

Aerosol is formed by mixing liquid or solid particles with a size of 0.001–100 μm randomly distributed in the air [1,2]. It can directly and indirectly affect the Earth's climate system. On the one hand, it directly affects the radiation balance of the Earth's climate system by scattering and absorbing solar radiation [3–6]; on the other hand, it can also become a cloud condensation nucleus to affect the generation and disappearance of clouds [7–9]. At the same time, the continuous development of industry, human activities, and fuel combustion have led to more serious aerosol pollution, and people are paying more and more attention to air quality [10,11]; thus, research on aerosol is of great significance.

At present, lidar is an active optical remote sensing device for effectively detecting aerosol; it can continuously and stably obtain the optical properties and spatiotemporal distribution characteristics of aerosol [12]. In recent years, many researchers have used lidar to study the optical properties and distribution of aerosol particles. Zhang Yinchao et al. established the fluorescence–Mie polarization lidar system to distinguish sand dust, mineral dust, and air pollution aerosols by using the customized fluorescence-to-Mie ratio and volume depolarization ratio to classify aerosol mixtures in combination with backward trajectory analysis [13]. Chen Chao et al. used polarization lidar to study the optical properties of aerosols and clouds under different weather conditions [14]. Wang Zhuang et al. used ground-based lidar and satellites to study air pollution during Beijing's National Day in 2019, quantifying the contributions of cross-regional transported unnatural dust and anthropogenic pollutants to Beijing's air quality [15].

Most of the previous studies have used a single lidar to observe and analyze aerosol, of which the representative areas were limited [16,17]. To obtain the optical characteristics

and distribution of atmospheric aerosols in a large area, this paper used three sets of aerosol lidar in the mega-city comprehensive meteorological observation experiment to explore the distribution differences of aerosol in different areas of Beijing and monitor the horizontal transport mechanism of aerosol in pollution events. In order to improve the inversion accuracy of the data product, the lidar and sun photometer data were combined to assist the estimation of lidar ratios. Aerosol types distributed over Beijing during experimental observations were analyzed and validated by multiple data sources. Meanwhile, the influence of meteorological conditions on the spatiotemporal evolution of aerosol particles was analyzed, and the lidar observations were combined with backward trajectory analysis, potential source contribution function (PSCF), and concentration-weighted trajectory (CWT) models to study aerosol sources.

2. Data and Methods

2.1. Research Area

Beijing is located in the North China Plain, respectively surrounded by the Yanshan and Taihang Mountains on the north and west sides. The three sets of lidar are located in Yanqing, Haidian, and Nanjiao of Beijing. The specific locations of the lidar are shown in Figure 1. Yanqing station has a higher terrain and a relatively good ecological environment. Haidian station and Nanjiao station are typical urban environments with many vehicles and frequent human activities.

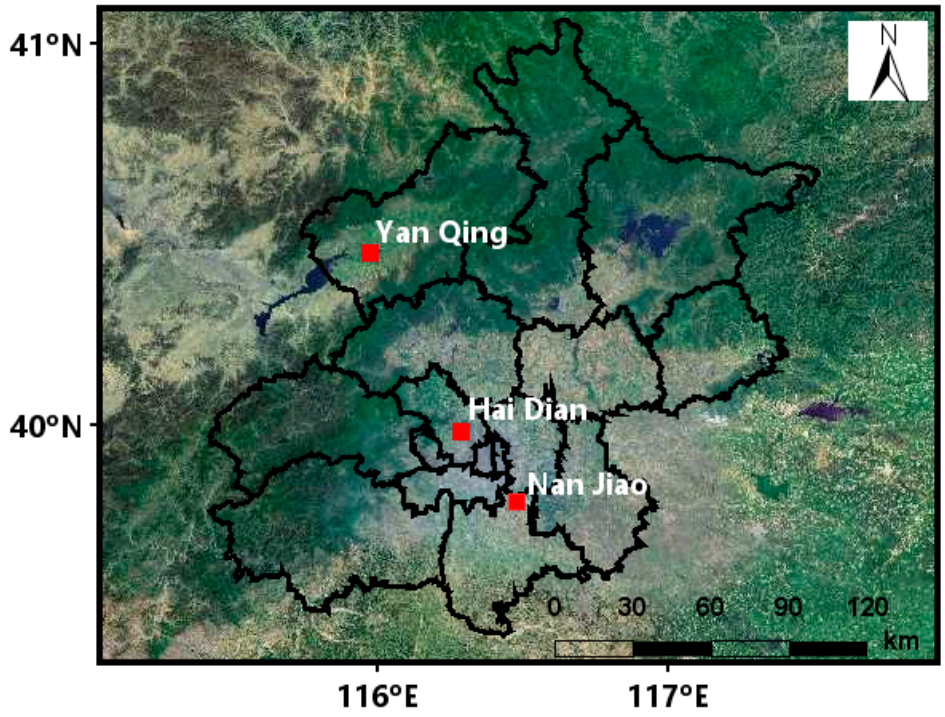

Figure 1. Location of Beijing lidar sites.

2.2. Aerosol Lidar Data

This paper uses the lidar of the comprehensive meteorological observation experiment in a mega-city (Yanqing, Haidian, and Nanjiao) for observation. The lidars at Yanqing and Nanjiao stations both use a 532 nm laser wavelength to achieve dual-channel detection of the parallel and vertical components of atmospheric aerosol backscattering light. The lidar at the Haidian site uses three different wavelengths which include 532 nm, 355 nm, and 1064 nm to achieve 5-channel simultaneous detection of aerosol optical parameters. Here, the lidars of the mega-city comprehensive meteorological observation experiment were validated in the network aerosol lidar calibration test, which was carried out by the Meteorological Observation Center of the China Meteorological Administration. The

calibration test for lidars is mainly divided into two steps. The first step of calibration mainly includes the self-calibration of the telescope alignment, the bottom noise of acquisition card, the received signal saturation, optical axis consistency, the Rayleigh scattering signal, and the retrieval algorithm with standard simulation data. Then, a comparison measurement by a calibrated lidar was carried out to verify the consistency of aerosol signals detected at the same location and space–time. Through the calibration, the relative system deviation of the original signal of the calibrated 532 nm-channel was reduced from 66.3% to 4.5% in the height range of 1–2 km, and from 65.5% to 4.3% in the height range of 2–5 km. The relative system deviation of the backscattering coefficient was reduced from 26.8% to 10.6% in the height range of 1–2 km, and from 137.3% to 17.6% in the height range of 2–5 km [18,19]. Afterwards, the data consistency was greatly improved, which provides a guarantee for the observation data used in this study. The observation continued 38 days from the opening ceremony of the Beijing Winter Olympics (4 February 2022) to the closing ceremony of the Winter Paralympics (13 March 2022).

The signal received by the lidar is the backscattering energy value of atmospheric molecules and aerosols. The optical characteristic parameters of the aerosol can be solved by the lidar equation. The lidar equation is as follows:

$$P(z) = C\frac{E}{Z^2}\beta(z)\exp\left[-2\int_0^z \alpha(z')dz'\right] \quad (1)$$

where $P(z)$ is the atmospheric backscattering echo power at the height z received by the lidar, E is the output energy of the lidar, C is the lidar system constant, $\beta(z)$ and $\alpha(z)$ is the total atmospheric backscattering coefficient and extinction coefficient.

In this paper, the Fernald algorithm is used to retrieve the lidar signal [20]. The equation of the method is as follows:

$$\alpha_a(r) = -\frac{S_a}{S_m}\alpha_m(z) + \frac{P(z)z^2\exp\left[2\left(\frac{S_a}{S_m}-1\right)\int_z^{z_c}\alpha_m(z')dz'\right]}{\frac{P(z_c){z_c}^2}{\alpha_a(z_c)+\frac{S_a}{S_m}\alpha_m(z_c)} + 2S_a\left\{\int_z^{z_c} P(z')z'^2\exp\left[-2\left(\frac{S_a}{S_m}-1\right)\int_z^{z_c}\alpha_m(z'')dz''\right]\right\}dz'} \quad (2)$$

where a and m represent aerosol and atmospheric molecules, respectively, α_a is the atmospheric aerosol extinction coefficient, α_m is the atmospheric molecules extinction coefficient, S_a is the lidar ratio of atmospheric aerosol, and S_m is the lidar ratio of atmospheric molecules, which is taken as $(8\pi)/3$ here.

The aerosol optical depth (AOD) can be obtained by integrating the extinction coefficient, and the calculation formula is as follows:

$$AOD = \int_0^Z \alpha_a(z)dz \quad (3)$$

2.3. Sun Photometer Data

AERONET is a ground-based aerosol remote sensing observation network, jointly established by NASA and LOA-PHOTONS (CNRS). AOD measured by sun photometer is usually considered as the true value, which is used to verify the remote sensing AOD. The distance between Beijing-CAMS (39.933° N, 116.371° E) and the lidar of Haidian station is less than 5 km. The CE-318 sun photometer data used in this paper are the AOD data of the 1.5-level product of the V3 version at a wavelength of 500 nm. The data can be found at NASA Goddard Space Flight Center (https://aeronet.gsfc.nasa.gov/, accessed on 10 March 2022).

2.4. CALIPSO Data

The CALIPSO satellite was launched from Vandenberg Air Force Base in California in 2006. It carries three instruments with zenith fields of view (CALIOP, IIR, WFC), which are mainly used to detect the vertical structure and characteristics of global clouds and aerosols, study the role of clouds and aerosols in regulating the Earth's climate, and study

the interaction between them [21,22]. This paper uses the V4.20 version of the aerosol-type feature stratification product from the CALIPSO L2 data, which is available at NASA Langley Research Center (https://search.earthdata.nasa.gov/, accessed on 4 March 2022).

2.5. Auxiliary Meteorological Data

Aerosol pollution is closely related to meteorological conditions. In this paper, the temperature, relative humidity, wind speed, wind direction, PM2.5, and PM10 data of the ground meteorological station at the same site as the lidar are selected to explore the influence of meteorological conditions on aerosol pollution. Here, the meteorological data are obtained from the Meteorological Observation Center of the China Meteorological Administration.

2.6. Backward Trajectory and Potential Source Analysis

The Centre for Atmosphere Watch and Services (CAWAS) and the Chinese Academy of Meteorological Science (CAMS) developed HYSPLIT follow-up software TrajSta. It was used to calculate the backward trajectories of air masses during aerosol pollution events during the Beijing Winter Olympics. The National Center for Environmental Prediction (NCEP) and Global Data Assimilation System (GDAS) data were used as the meteorological data input to calculate the backward trajectory of air masses in aerosol pollution events during the Beijing Winter Olympics (ftp://arlftp.arlhq.noaa.gov/pub/archives/, accessed on 10 March 2022). Taking the position of Beijing (39.9° N, 116.3° E) as the starting point and 500 m as the starting height, the 24 h backward trajectory analysis was carried out for the air mass source of the external transmission event every hour. Based on the results of the backward trajectory analysis, a PM10 concentration equal to 100 $\mu g/m^3$ was taken as the pollutant threshold for the first pollution event, and a PM2.5 concentration equal to 75 $\mu g/m^3$ was taken as the pollutant threshold for the second pollution event, utilizing the potential source contribution function (PSCF) and concentration-weighted trajectory (CWT) models to further determine the source and location of pollutants [23].

3. Results and Discussion

3.1. Calculation of Lidar Ratio

The ratio of particle extinction coefficient to backscattering coefficient is defined as the lidar ratio, which is an important parameter for characterizing atmospheric aerosols [24]. The lidar ratio needs to be assumed when retrieving lidar data. Most studies often use the lidar ratio empirical value of 50 sr at 532 nm, which causes deviations in the results. In this paper, the average lidar ratio in the vertical direction at 532 nm is derived by combining the data of the sun photometer and lidar, which avoids the assumption of important parameters and improves the accuracy of data inversion [25,26].

The AOD measured by the sun photometer is the total atmospheric optical depth, which is expressed as. Then, the optical depth of the aerosol measured by the sun photometer can be expressed as follows:

$$S_A = S_T - \int_{r_z}^{\infty} \alpha_a(r)dr - \int_0^{\infty} \alpha_m(r)dr \quad (4)$$

where r_z is the height of the reference point selected during the retrieval of the backscattering coefficient by lidar.

The area where the height of the reference point was selected was dominated by atmospheric molecules, and the vast majority of aerosol particles were gathered below this height; thus, the above equation can be simplified as:

$$S_A = S_T - \int_0^{\infty} \alpha_m(r)dr \quad (5)$$

The equation for calculating the optical depth of the lidar is expressed as follows:

$$L_A = \int_0^{r_z} S_a \cdot \beta_a(r) dr \quad (6)$$

where S_a is the lidar ratio of aerosol, and Equation (7) holds:

$$S_A = L_A = \int_0^{r_z} S_a \cdot \beta_a(r) dr,\ S_a \in [10, 100] \quad (7)$$

For the calculation of the lidar ratio, it was assumed that the lidar ratio of aerosol gradually increased from 10 sr to 100 sr with an increment interval of 1 sr in the process of retrieving the AOD from lidar data. Then, the optical depth of atmospheric molecules was subtracted from the AOD obtained by the sun photometer. Finally, the estimated lidar ratio corresponded to the minimum relative deviation of the AOD measured by the lidar and the sun photometer. The specific calculation process is shown in Figure 2.

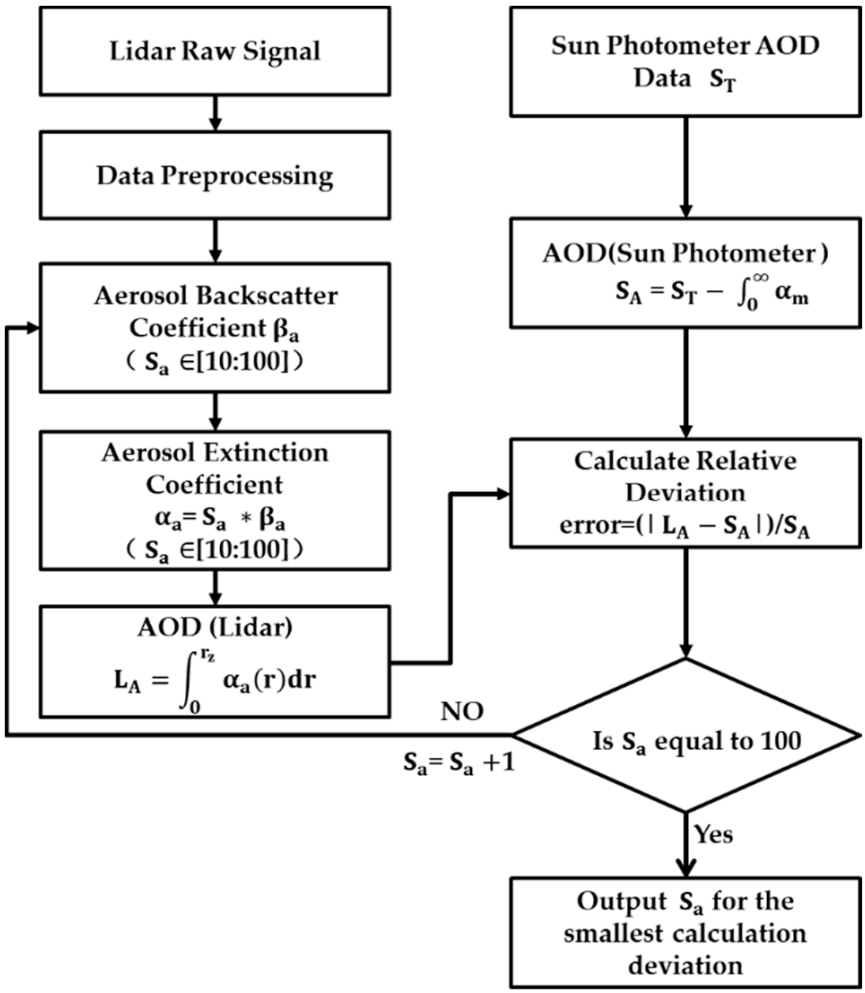

Figure 2. Flow chart of calculating aerosol lidar ratio.

The error between the AOD measurement obtained from the multi-channel sun photometer at a wavelength of 500 nm and the AOD value measured by the lidar at 532 nm is negligible. The calculated results are shown in Figure 3.

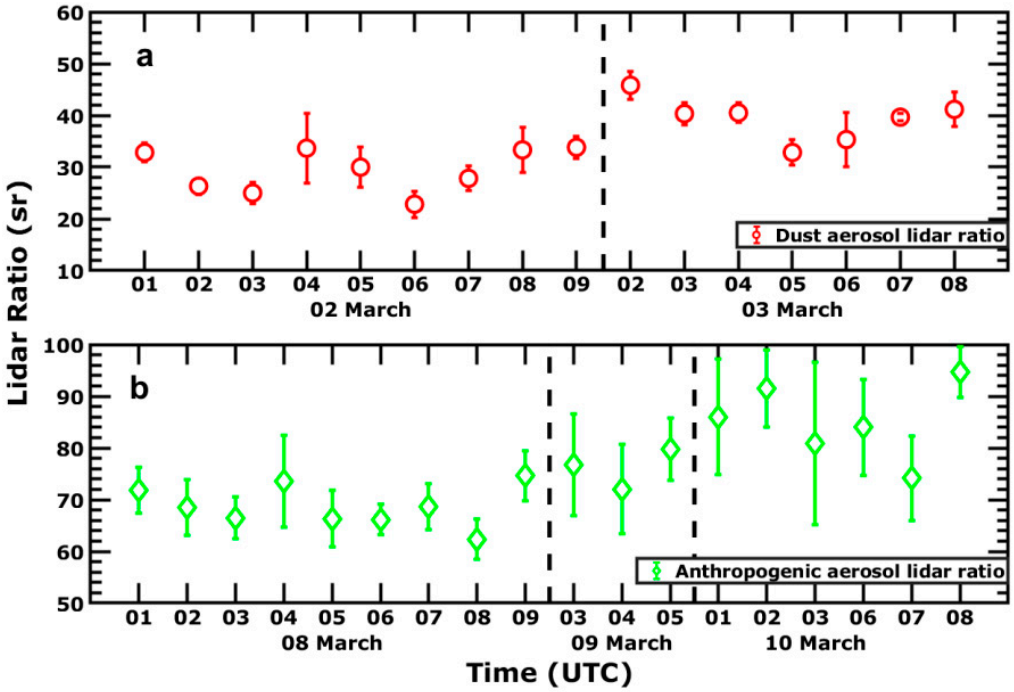

Figure 3. Results of aerosol lidar ratio calculated by lidar combined with sun photometer ((**a**) the dust aerosol lidar ratio; (**b**) the anthropogenic aerosol lidar ratio).

In Figure 3, it is shown that the average lidar ratio from 2 to 3 March was 34 ± 3 sr, and the lidar ratio was small due to the impact of dust; this is also consistent with the previous study in which Beijing had a lidar ratio of 36.2 ± 4.7 sr during the period of dust [27]. The average lidar ratio from 8 to 10 March was 75 ± 7 sr, which is relatively large. Note that a lidar ratio that is greater than 60 sr is often affected by anthropogenic aerosols [28].

3.2. Vertical Distribution Characteristics of Aerosol during the Winter Olympics

In order to further study the pollutant concentration and the vertical distribution of aerosols in different regions during the Winter Olympics, the aerosol extinction coefficient and PM data of each site were averaged monthly. It can be seen from Figure 4a,c,e that the average value of the PM2.5 and PM10 data of each region is greater in March than that in February, which may be related to the multiple occurrences of aerosol pollution events in March. The PM2.5/PM10 ratio of 50% is the dividing line between natural pollution and manmade pollution [29–31]. The ratio of each station area in February and March has always remained above 55.17%, and the highest it reached was 86.77%. This reflects that the Beijing area is mainly affected by anthropogenic pollution, and the concentration of fine particles pollutants is relatively high. In addition, there are differences in the spatial distribution of the ratio of PM2.5/PM10. Among them, the ratios of Haidian and Nanjiao are higher than 70%, which is closely related to the dense population and serious anthropogenic pollution in Haidian and Nanjiao.

Figure 4b,d,f shows the vertical distribution of the monthly average aerosol extinction coefficient of each lidar station in February and March. The average values of the aerosol extinction coefficients below 1 km (around the boundary layer height) from high to low are: Nanjiao > Haidian > Yanqing and Haidian > Nanjiao > Yanqing. The overall spatial distribution is high in the southeast and low in the northwest. Such a difference in spatial distribution is directly related to the planning of Beijing's urban functional areas. Haidian is the functional core area of the capital with a prosperous economy and frequent human activities, where the massive emission of anthropogenic aerosols causes a high extinction coefficient near the ground. The Nanjiao site is located in DaXing, which is a new urban development area, and its southern part is close to many traditional industrial cities; in

addition, Nanjiao is close to the South Fifth Ring Road with a large traffic flow, where the transport of pollutants between regions and the emission of vehicle exhaust could also cause differences in the spatial distribution of extinction coefficients. Yanqing is mainly an ecological conservation and development area with a good ecological environment and low pollution, so the bottom layer has a low extinction coefficient.

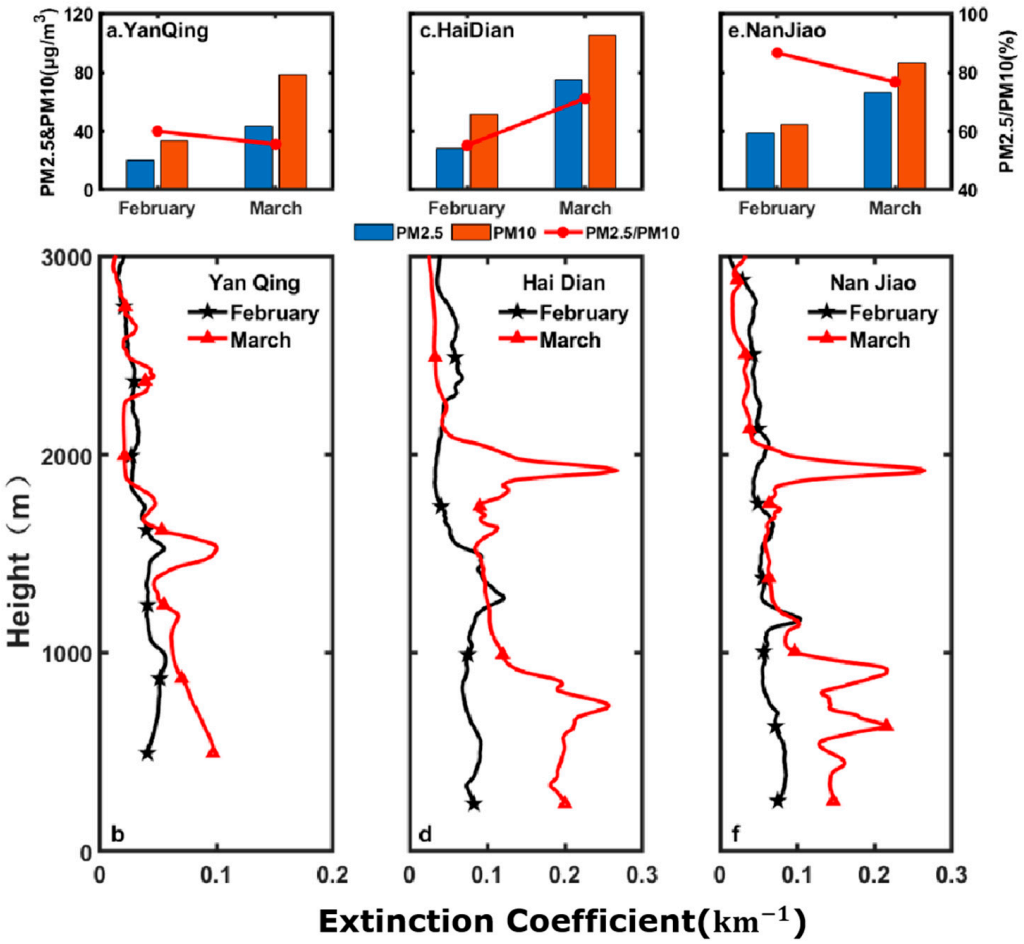

Figure 4. Monthly averaged PM data and extinction coefficient profiles at each station during the Winter Olympics.

As one of the three major competition areas of the Winter Olympics, Yanqing mainly carries out outdoor competitions such as snowmobiles, sleds, and alpine skiing. By analyzing the vertical structure of the monthly average values of PM and extinction coefficients in Yanqing, it is found that the Yanqing competition area has the advantages of a low pollutant concentration and sunny weather with few clouds, which are conducive to the smooth development of outdoor competitions and the successful completion of the Winter Olympics.

3.3. Observation and Analysis of Dust Weather Process

Three lidars in Beijing simultaneously monitored an aerosol pollution event from 2 to 4 March. As shown in Figure 5, the aerosol layer with an extinction coefficient of 0.6 km^{-1} was observed at the three stations at the same time from 15:00 to 16:00 on 3 March, indicating that there was a high concentration of pollutants entering the Beijing area at this time. The bottom of the aerosol layer in Figure 5b Haidian and Figure 5c Nanjiao were about 1 km high. Due to the high altitude of Yanqing in Figure 5a, the bottom of the aerosol layer was about 0.6 km. At 16:00, there was a low wind speed in the Beijing area (the wind speeds in the three regions of Figure 8a–c were about 2 m/s), and the aerosol layer

began to sink gradually. At 0:00 on 4 March, the extinction coefficient of aerosol in Yanqing dropped to a minimum value of 0.17 km^{-1}. At 02:00 on 4 March, the aerosol extinction coefficients in Haidian and Nanjiao dropped to the minimum of 0.3 km^{-1}, indicating that the aerosol imported from outside area had settled to the ground and mixed with local aerosols. Beginning at 02:00 on 4 March, there was a relatively high wind speed near the ground in the Beijing area (the minimum wind speed in the three regions of Figure 8a–c was about 16 m/s), and the near-ground aerosol was rapidly diffused into the air; afterwards, the extinction coefficient of the aerosol in Yanqing was 0.23 km^{-1}. At 03:00 on 4 March, the aerosol extinction coefficients in Haidian and Nanjiao were about 0.49 km^{-1}, and the high wind speeds promoted the diffusion of pollutants near the ground. Then at 04:00 on 4 March, the near-ground extinction coefficient in the Beijing area reached the minimum value, about 0.09 km^{-1}.

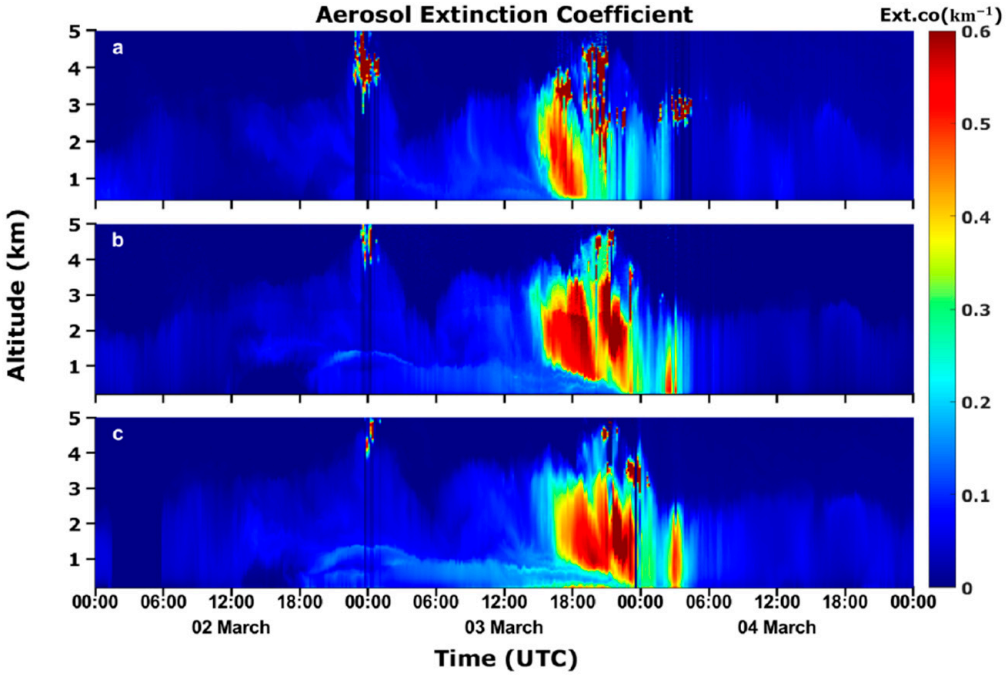

Figure 5. The spatiotemporal distribution of extinction coefficients in each region ((**a**) Yanqing, (**b**) Haidian, and (**c**) Nanjiao).

In Figure 6, the depolarization ratios of particles in the three regions were between 0.15 and 0.35 during 2–4 March, indicating that the shape of aerosol particles tends to be non-spherical. In particular, from 15:00 on 3 March to 03:00 on 4 March, the particle depolarization ratio of the aerosol layer usually exceeded 0.26. During aerosol pollution events, the depolarization ratio of particles greater than 0.2 can be considered as dust particles [13]. The particle depolarization ratios of dust and polluted dust are 0.2–0.42 and 0.15–0.26, respectively [32].

Due to the different locations of the three lidar sites, it can be seen from Figure 1 that the three lidars are located on a straight line from the northwest to the southeast; therefore, according to the characteristics of this location, this paper makes a rough analysis of the aerosol sourcing direction. After making an average and normalization of the extinction coefficient profile of the three regions in Figure 5, the results are shown in Figure 7. The height range of 1.7–2 km, where the extinction coefficient suddenly increased, is focused on for further analysis.

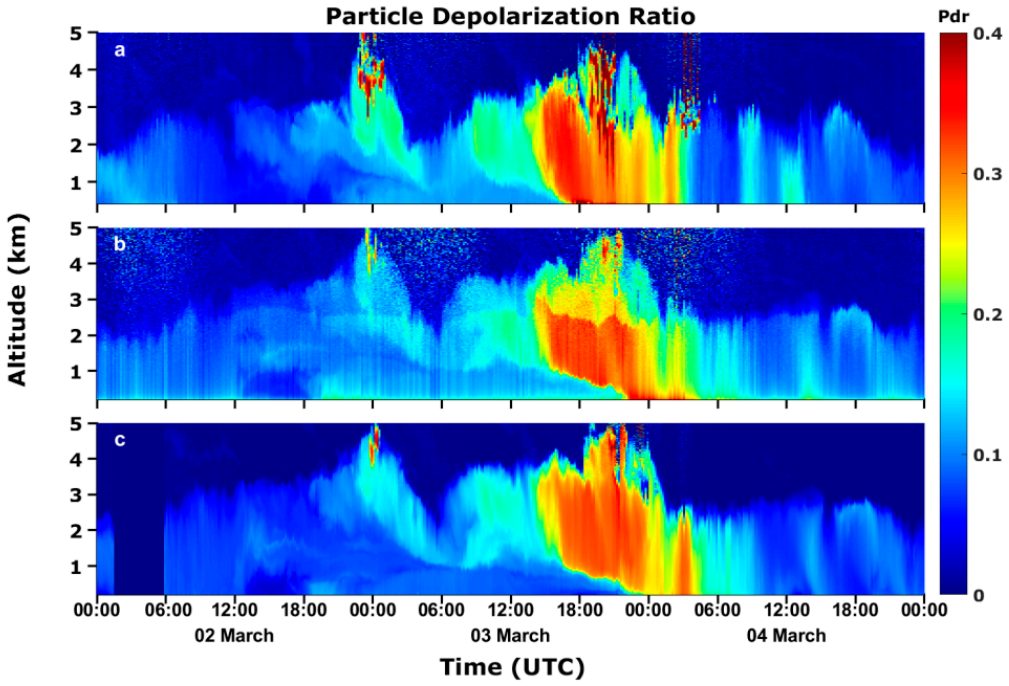

Figure 6. The spatiotemporal distribution of particle depolarization ratios in each region ((**a**) Yanqing, (**b**) Haidian, and (**c**) Nanjiao).

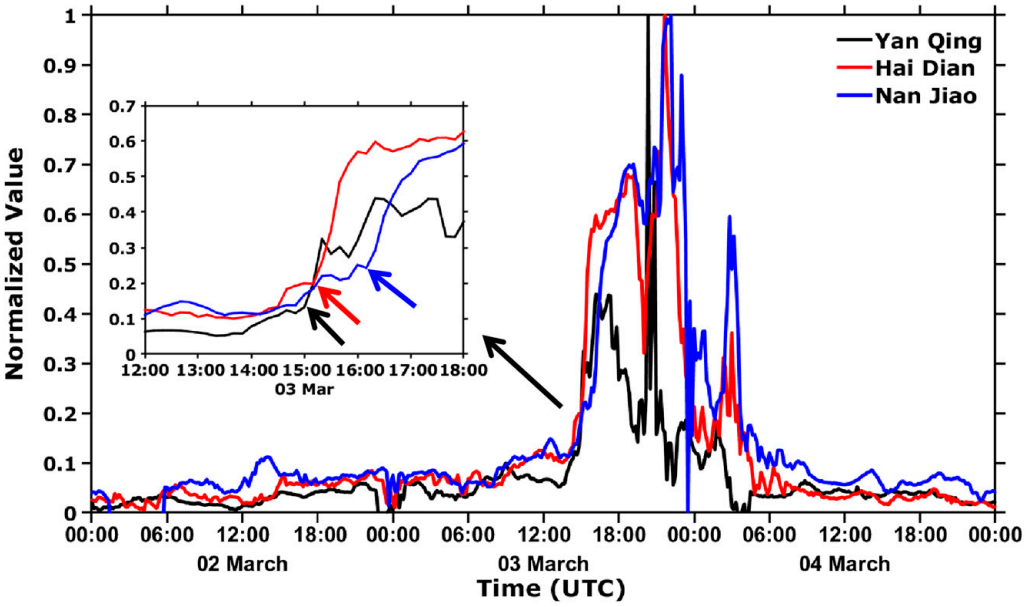

Figure 7. Normalized results of the average value of extinction coefficients in the 1.7–2 km height range of each region.

By enlarging the normalized profiles from 12:00 to 18:00 on 3 March, it is found that the extinction coefficients of the three regions all suddenly increased at a certain time node, indicating a moment of a large amount of aerosol input. It can be observed from the enlarged map that the time points of the sudden increases in different regions show a discrepancy. In particular, the time sequence is Yanqing–Haidian–Nanjiao, which also corresponds to the location of the three lidars from northwest to southeast. By combining this time sequence with the related geographical location characteristics, it can be preliminarily deduced that the input air mass of this aerosol originated in the west or north of Beijing. As shown in Figure 8, the frequent occurrence of western or northern winds during the whole aerosol pollution process can also reasonably explain this conclusion.

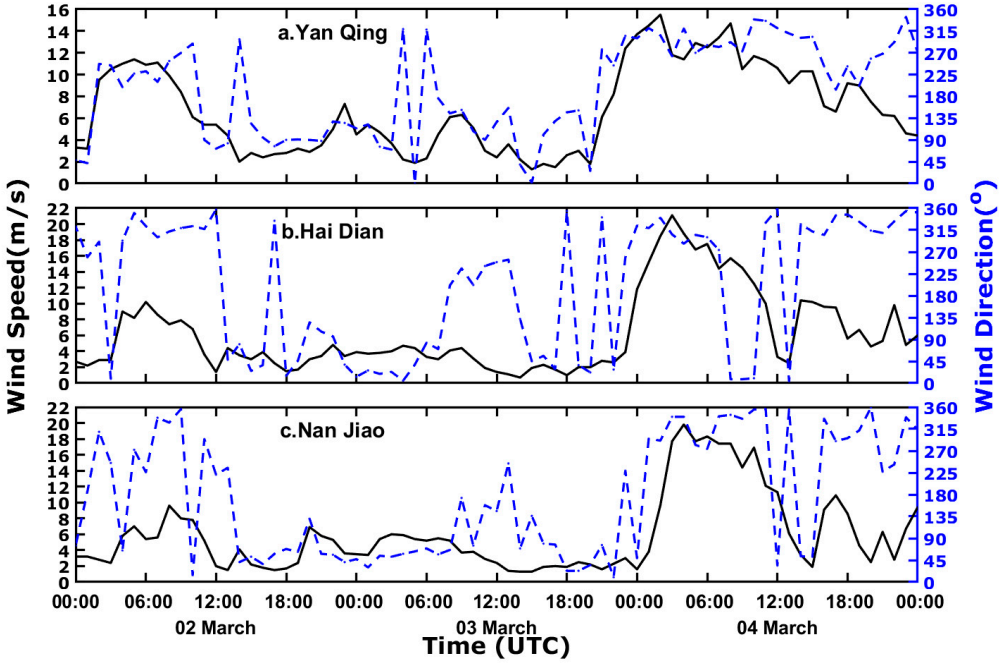

Figure 8. Wind speed and direction on the surface of each region ((**a**) Yanqing, (**b**) Haidian, and (**c**) Nanjiao).

Figure 9 shows the observation results of the CALIPSO satellite when it passed over the area around Beijing on 4 March. It was found that the aerosol types around Beijing were mainly dust and polluted dust aerosols, which indirectly shows that the diameters of the aerosol particles were relatively large. Therefore, the PM10 data will be the input of pollutants for subsequent calculations of PSCF and CWT.

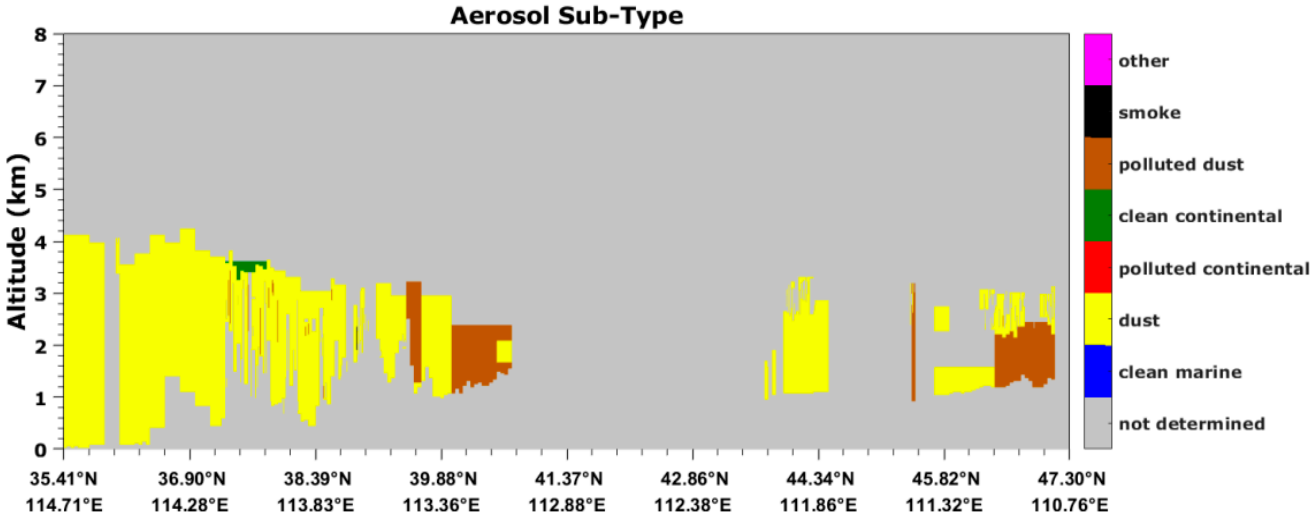

Figure 9. Distribution of aerosol types on 4 March.

Figure 10a shows the probability of occurrence of 24 h backward trajectory clusters 1–4, which are 33.33%, 29.17%, 20.83%, and 16.67%, respectively. Most of the trajectories come from Mongolia and Inner Mongolia. As shown in Figure 10b,c, WPSCF shows that the most probable source regions are mainly concentrated in Mongolia, Inner Mongolia, and Hebei–Shanxi border areas with WCWT values higher than 60 $\mu g/m^3$, indicating that the corresponding regions contributed a large amount of PM10 to the pollution in Beijing.

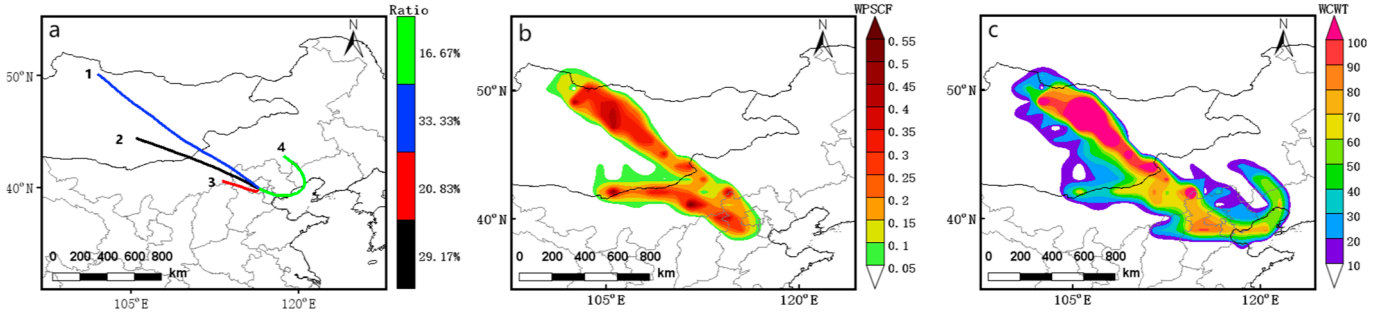

Figure 10. Spatial distribution of clusters by backward air mass trajectories, WPSCF, and WCWT ((**a**) Backward air mass trajectories; (**b**) WPSCF; (**c**) WCWT).

3.4. Observation and Analysis of Haze Weather Process

Three lidars in Beijing observed the process of aerosol deposition and diffusion from 8 to 11 March. As shown in Figure 11, the deposition process of aerosols began at about 06:00 on 9 March, and the extinction coefficient of the near-ground aerosol gradually increased. At about 23:00 on 9 March, the extinction coefficients near the ground in the three regions reached the maximum values, all greater than 0.8 km^{-1}. As shown in Figures 12 and 13, the relative humidity of the three regions was greater than 80% and the wind speed was less than 2 m/s, which limited the diffusion of aerosols. The diffusion process began at 23:00 on 10 March, and the extinction coefficients near the ground gradually decreased. At 08:00 on 11 March, the extinction coefficients near the ground reached the minimum values, which were less than 0.3 km^{-1}. At this time, the relative humidity of the three regions was less than 40% and, the wind speed was greater than 4 m/s, which promoted the diffusion of aerosols.

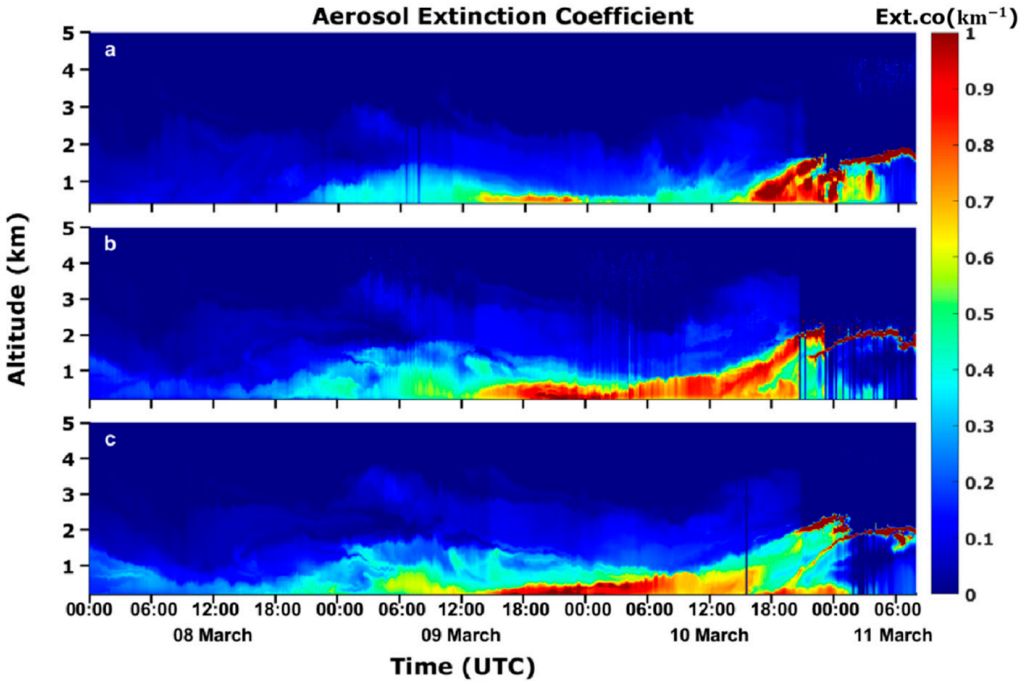

Figure 11. The spatiotemporal distribution of extinction coefficients in each region ((**a**) Yanqing, (**b**) Haidian, and (**c**) Nanjiao).

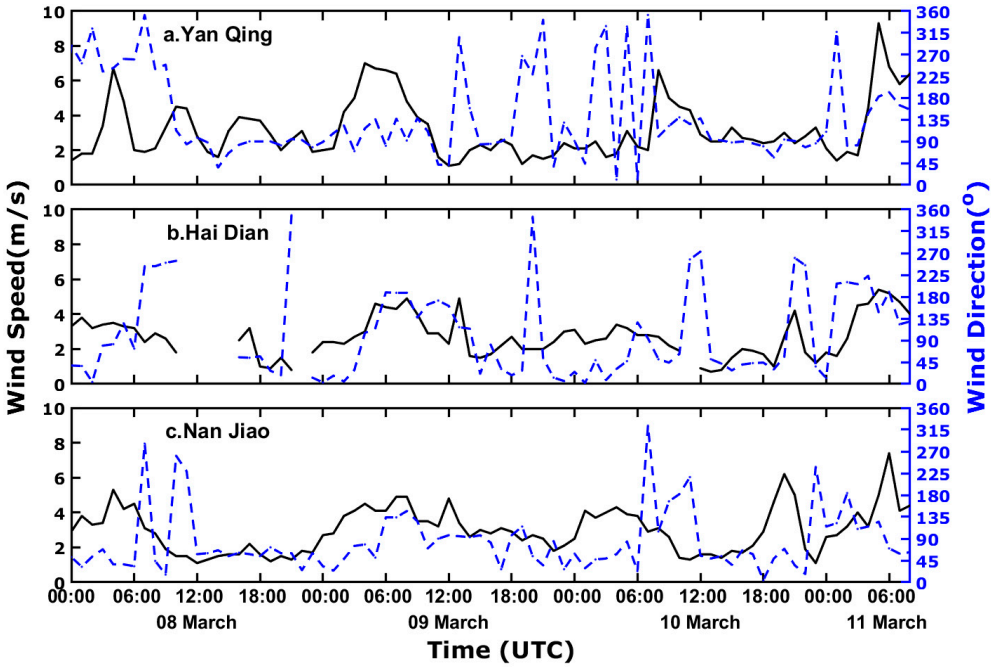

Figure 12. Wind speed and direction on the surface of each region ((**a**) Yanqing, (**b**) Haidian, and (**c**) Nanjiao).

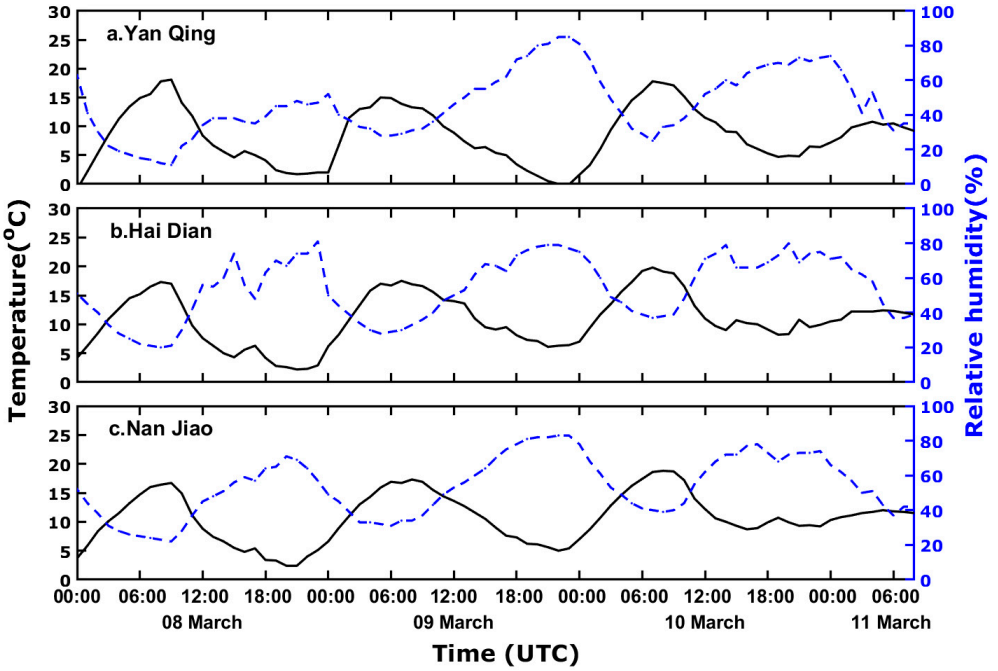

Figure 13. Temperature and humidity on the surface of each region ((**a**) Yanqing, (**b**) Haidian, and (**c**) Nanjiao).

Combining Figures 11 and 14, it is found that the particle depolarization ratio is less than 0.1 in the region where the extinction coefficient is greater than 0.5, indicating that the particle shapes with higher particle concentration tend to be spherical. Previous studies have shown that the particle depolarization ratio of anthropogenic aerosol pollution in Beijing is between 0.05 and 0.12 [13], indicating that the type of aerosol pollution is mainly anthropogenic aerosol, so the PM2.5 data are the input as pollutants for analysis in the subsequent calculations of PSCF and CWT.

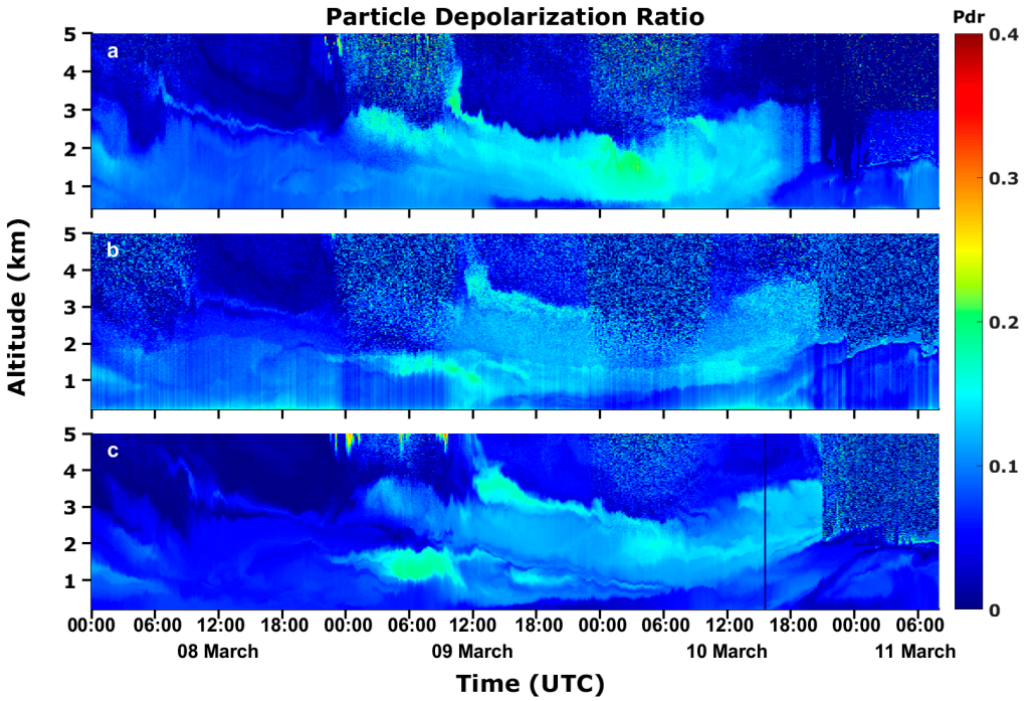

Figure 14. The spatiotemporal distribution of particle depolarization ratio in each region ((**a**) Yanqing, (**b**) Haidian, and (**c**) Nanjiao).

Figure 15a shows the probability of occurrence of 24 h backward trajectory clusters 1–3, which are 18.06%, 40.28%, and 41.67%, respectively. Most of the trajectories come from Tianjin, Bohai Bay, and southern Hebei in the east and south of Beijing. As shown in Figure 15b,c, WPSCF shows that the most probable source regions are mainly concentrated in southeastern Beijing, southern Hebei, and Tianjin with WCWT values higher than 100 μg/m^3, indicating that the corresponding regions contributed a large amount of PM2.5 to the pollution in Beijing.

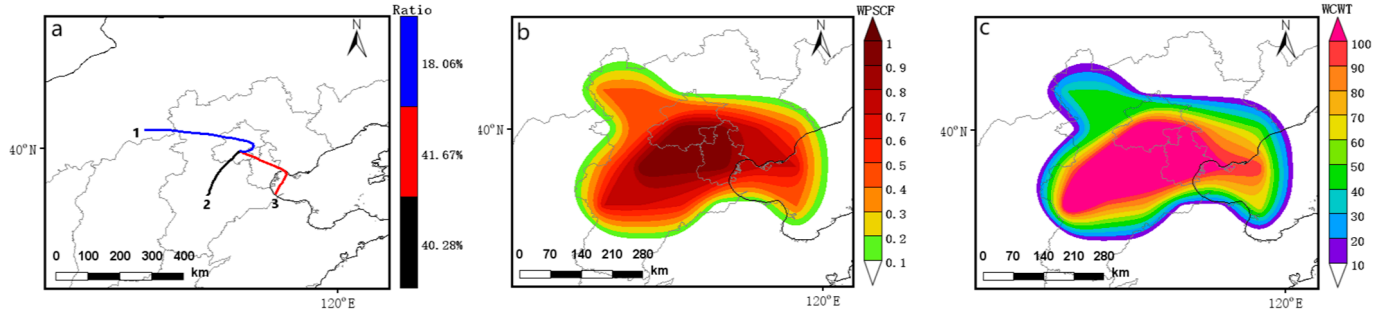

Figure 15. Spatial distribution of clusters by backward air mass trajectories, WPSCF, and WCWT ((**a**) Backward air mass trajectories; (**b**) WPSCF; (**c**) WCWT).

4. Conclusions

The multiple optical parameters of Beijing's aerosol pollution were obtained through data inversion, and the optical properties and vertical distribution of aerosol in different regions of Beijing were analyzed in detail, using lidars in three different regions of Beijing during the Winter Olympics. Combining these data with the sun photometer data, the lidar ratio was determined; the type of aerosol was determined by using the observations of the CALIPSO satellite; and the source of the aerosol particles was identified by the backward trajectory of the air mass and the PSCF and CWT models. The results of this study are summarized below:

1. The PM2.5, PM10, and the aerosol extinction coefficients in the three regions are generally lower in February than in March, and the overall spatial distribution showed a distribution pattern of higher concentration in the southeast and lower in the northwest. This difference is mainly due to differences in topography and economic activities.
2. The determination of the lidar ratio was retrieved through the observation data obtained by lidar and sun photometer. The lidar ratio of the first aerosol pollution event was smaller than the second aerosol pollution event due to the transmission of dust aerosol in the northwest direction.
3. The aerosol type of the first pollution event was mainly dust aerosol. On 2 March, the northwest wind brought aspherical dust particles into Beijing. During the night of 3 March, the lower wind speed caused the deposition of aerosol particles, which aggravated the aerosol pollution near the ground. On the morning of 4 March, higher wind speeds promoted the diffusion of near-ground aerosol.
4. The aerosol type of the second pollution event was mainly anthropogenic aerosols. Meteorological conditions have a great impact on anthropogenic aerosol pollution. From the night of 9 March to the morning of 10 March, the ground extinction coefficient was relatively large, which may be related to the high relative humidity and low wind speed. On the night of the 11 March and the morning of the 11 March, the high wind speed and low relative humidity led to the separation of the upper aerosol and the ground aerosol, and the extinction coefficient near the ground decreased.
5. Under adverse weather conditions, the causes of aerosol pollution in Beijing can be mainly divided into two aspects: the transportation of dust aerosol particles in the northwest direction and the emission of anthropogenic aerosol particles in the local and surrounding cities. Therefore, the control of air quality should not only focus on local energy conservation and emission reduction, but also pay attention to the transportation of regional air pollutants.

Author Contributions: Conceptualization, T.L. and Z.L.; methodology, T.L. and Z.L.; validation, Z.L. and Y.C.; formal analysis, T.L. and Z.L.; investigation, Z.B.; resources, Z.B.; data curation, X.W.; writing—original draft preparation, T.L.; writing—review and editing, Z.L. and Y.C.; visualization, Z.L. and Y.C.; supervision, X.W.; project administration, Z.L. and Y.C.; funding acquisition, Z.L. and Y.C. All authors have read and agreed to the published version of the manuscript.

Funding: This research was jointly supported by the National key R&D plan of China (2017YFC1501701), the National Natural Science Foundation of China (40905005 and 41675028), and the Natural Science Foundation of Shandong Province (ZR2021MD112).

Institutional Review Board Statement: Not applicable.

Informed Consent Statement: Not applicable.

Data Availability Statement: The publicly available datasets used in this paper are as follows: Sun photometer data can be found from the link: https://aeronet.gsfc.nasa.gov/ (accessed on 2–3 March 2022 and 8–10 March 2022), Calipaso data can be found from the link: https://search.earthdata.nasa.gov/ (accessed on 4 March 2022) and GDAS data can be found from the link: ftp://arlftp.arlhq.noaa.gov/pub/archives/gdas1/ (accessed on 2–4 March 2022 and 8–11 March 2022).

Acknowledgments: Special thanks to the Meteorological Observation Center of China Meteorological Administration for providing the lidar data and ground station data. Thanks to NASA Goddard Space Flight Center for the sun photometer data, NASA Langley Research Center for the Calipso data, the National Center for Environmental Prediction (NCEP) for the GDAS data, and (CAWAS) and (CAMS) for the HYSPLIT follow-up software TrajSta.

Conflicts of Interest: The authors declare no conflict of interest.

References

1. Pope, C.A., 3rd; Dockery, D.W. Health effects of fine particulate air pollution: Lines that connect. *J. Air Waste Manag. Assoc.* **2006**, *56*, 709–742. [CrossRef] [PubMed]
2. Wu, X.; Xin, J.; Zhang, W.; Gong, C.; Ma, Y.; Ma, Y.; Wen, T.; Liu, Z.; Tian, S.; Wang, Y.; et al. Optical, Radiative and Chemical Characteristics of Aerosol in Changsha City, Central China. *Adv. Atmos. Sci.* **2020**, *37*, 1310–1322. [CrossRef]
3. Choi, J.; Son, S.-W.; Park, R.J. Aerosol versus greenhouse gas impacts on Southern Hemisphere general circulation changes. *Clim. Dyn.* **2018**, *52*, 4127–4142. [CrossRef]
4. Gryspeerdt, E.; Quaas, J.; Ferrachat, S.; Gettelman, A.; Ghan, S.; Lohmann, U.; Morrison, H.; Neubauer, D.; Partridge, D.G.; Stier, P.; et al. Constraining the instantaneous aerosol influence on cloud albedo. *Proc. Natl. Acad. Sci. USA* **2017**, *114*, 4899–4904. [CrossRef] [PubMed]
5. Singh, D.; Bollasina, M.; Ting, M.; Diffenbaugh, N.S. Disentangling the influence of local and remote anthropogenic aerosols on South Asian monsoon daily rainfall characteristics. *Clim. Dyn.* **2018**, *52*, 6301–6320. [CrossRef]
6. Zhang, Y.; Xu, D.; He, Q.; Li, D.; Qin, K. Vertical distribution and regional transport analysis of aerosols in Zhejiang Province. *Chin. Environ. Sci.* **2021**, *41*, 11.
7. Leonardi, A.; Ricker, H.M.; Gale, A.G.; Ball, B.T.; Odbadrakh, T.T.; Shields, G.C.; Navea, J.G. Particle formation and surface processes on atmospheric aerosols: A review of applied quantum chemical calculations. *Int. J. Quantum Chem.* **2020**, *120*, e26350. [CrossRef]
8. Kim, D.; Ramanathan, V. Solar radiation budget and radiative forcing due to aerosols and clouds. *J. Geophys. Res.* **2008**, *113*, 8434. [CrossRef]
9. Solomos, S.; Bougiatioti, A.; Soupiona, O.; Papayannis, A.; Mylonaki, M.; Papanikolaou, C.; Argyrouli, A.; Nenes, A. Effects of regional and local atmospheric dynamics on the aerosol and CCN load over Athens. *Atmos. Environ.* **2019**, *197*, 53–65. [CrossRef]
10. Salam, A.; Mamoon, H.A.; Ullah, M.B.; Ullah, S.M. Measurement of the atmospheric aerosol particle size distribution in a highly polluted mega-city in Southeast Asia (Dhaka-Bangladesh). *Atmos. Environ.* **2012**, *59*, 338–343. [CrossRef]
11. Che, H.; Xia, X.; Zhu, J.; Wang, H.; Wang, Y.; Sun, J.; Zhang, X.; Shi, G. Aerosol optical properties under the condition of heavy haze over an urban site of Beijing, China. *Environ. Sci. Pollut. Res.* **2015**, *22*, 1043–1053. [CrossRef] [PubMed]
12. Comeron, A.; Munoz-Porcar, C.; Rocadenbosch, F.; Rodriguez-Gomez, A.; Sicard, M. Current Research in Lidar Technology Used for the Remote Sensing of Atmospheric Aerosols. *Sensors* **2017**, *17*, 1450. [CrossRef] [PubMed]
13. Zhang, Y.; Sun, Z.; Chen, S.; Chen, H.; Guo, P.; Chen, S.; He, J.; Wang, J.; Nian, X. Classification and source analysis of low-altitude aerosols in Beijing using fluorescence–Mie polarization lidar. *Opt. Commun.* **2021**, *479*, 126417. [CrossRef]
14. Chen, C.; Song, X.; Wang, Z.; Wang, W.; Wang, X.; Zhuang, Q.; Liu, X.; Li, H.; Ma, K.; Li, X.; et al. Observations of Atmospheric Aerosol and Cloud Using a Polarized Micropulse Lidar in Xi'an, China. *Atmosphere* **2021**, *12*, 796. [CrossRef]
15. Wang, Z.; Liu, C.; Dong, Y.; Hu, Q.; Liu, T.; Zhu, Y.; Xing, C. Profiling of Dust and Urban Haze Mass Concentrations during the 2019 National Day Parade in Beijing by Polarization Raman Lidar. *Remote Sens.* **2021**, *13*, 3326. [CrossRef]
16. Qiu, X.; An, X.; Liu, B.; Lu, H.; Wang, X.; Wang, Q.; Luo, X. Discussion on the vertical characteristics and influencing factors of aerosol extinction coefficients in Beijing. *Environ. Sci. Res.* **2020**, *33*, 7.
17. Li, Z.; Xie, Y.; Zhang, Y.; Li, L.; Xu, H.; Li, K. Research progress on remote sensing of atmospheric aerosol components. *J. Remote Sens.* **2019**, *23*, 15.
18. Chen, Y.; Wang, X.; Bu, Z.; Wang, Y.; Guo, Z.; Xiong, F.; Wang, X. Megacity test aerosol laser radar standard and result analysis. *Laser Technol.* **2022**, *46*, 435.
19. Bu, Z.; Wang, X.; Wang, Y.; Liu, J.; Chen, Y. Comparison and Analysis of Aerosol Lidar Network in Mega City of Beijing Using Real Lidar. In Proceedings of the 2019 International Conference on Meteorology Observations (ICMO), Chengdu, China, 28–31 December 2019; pp. 1–3.
20. Fernald, F.G. Analysis of atmospheric lidar observations: Some comments. *Appl. Opt.* **1984**, *23*, 652–653. [CrossRef]
21. Solanki, R.; Singh, N. LiDAR observations of the vertical distribution of aerosols in free troposphere: Comparison with CALIPSO level-2 data over the central Himalayas. *Atmos. Environ.* **2014**, *99*, 227–238. [CrossRef]
22. Reddy, K.R.O.; Zhang, X.; Bi, L. Seasonal aerosol variations over a coastal city, Zhoushan, China from CALIPSO observations. *Atmos. Res.* **2019**, *218*, 117–128. [CrossRef]
23. Fan, W.; Qin, K.; Xu, J.; Yuan, L.; Li, D.; Jin, Z.; Zhang, K. Aerosol vertical distribution and sources estimation at a site of the Yangtze River Delta region of China. *Atmos. Res.* **2019**, *217*, 128–136. [CrossRef]
24. Müller, D.; Ansmann, A.; Mattis, I.; Tesche, M.; Wandinger, U.; Althausen, D.; Pisani, G. Aerosol-type-dependent lidar ratios observed with Raman lidar. *J. Geophys. Res.* **2007**, *112*, D16. [CrossRef]
25. Müller, D.; Lee, K.H.; Gasteiger, J.; Tesche, M.; Weinzierl, B.; Kandler, K.; Müller, T.; Toledano, C.; Otto, S.; Althausen, D.; et al. Comparison of optical and microphysical properties of pure Saharan mineral dust observed with AERONET Sun photometer, Raman lidar, and in situ instruments during SAMUM 2006. *J. Geophys. Res. Atmos.* **2012**, *117*, 16825. [CrossRef]
26. Papayannis, A.; Amiridis, V.; Mona, L.; Tsaknakis, G.; Balis, D.; Bösenberg, J.; Chaikovski, A.; De Tomasi, F.; Grigorov, I.; Mattis, I.; et al. Systematic lidar observations of Saharan dust over Europe in the frame of EARLINET (2000–2002). *J. Geophys. Res.* **2008**, *113*, 9028. [CrossRef]
27. Xie, C.; Nishizawa, T.; Sugimoto, N.; Matsui, I.; Wang, Z. Characteristics of aerosol optical properties in pollution and Asian dust episodes over Beijing, China. *Appl. Opt.* **2008**, *47*, 4945–4951. [CrossRef]

28. Cattrall, C.; Reagan, J.; Thome, K.; Dubovik, O. Variability of aerosol and spectral lidar and backscatter and extinction ratios of key aerosol types derived from selected Aerosol Robotic Network locations. *J. Geophys. Res. Atmos.* **2005**, *110*, 5124. [CrossRef]
29. Yang, W.T.; Yao, S.Q.; Deng, M.; Wang, Y.J. Spatio-temporal Distribution Characteristics of PM2.5 and Spatio-temporal Variation Characteristics of the Relationship Between PM2.5 and PM10 in Beijing. *Environ. Sci.* **2017**, *39*, 684–690.
30. Deng, F.R.; Kang, N.; Kang, H.U.; Jiang, Y.C.; Na, Y.X.J.C.E.S. Analysis of air pollution episodes over different cites in the Yangtze River Delta. *Chin. Environ. Sci.* **2018**, *38*, 401–411.
31. Li, M.; He, Y. Spatial and temporal distribution characteristics of PM(2.5)/PM(10) in the atmospheric environment of Shanghai. *J. Yunnan Univ.* **2019**, *41*, 323–332.
32. Chen, S.; Nian, X.; Chen, H.; Zhang, Y.; Guo, P.; Bu, Z. Observation and analysis of optical characteristics of aerosols in the pollution process in urban Area of Beijing. *Opt. Technol.* **2021**, *47*, 570–576.